$FeNi_3/NiFeO_x$ Nanohybrids as Highly Efficient Bifunctional Electrocatalysts for Overall Water Splitting

Xiaodong Yan, Lihong Tian, Kexue Li, Samuel Atkins, Haifeng Zhao, James Murowchick, Lei Liu, and Xiaobo Chen**

Earth-abundant, low-cost, and highly active bifunctional electrocatalysts are of significant importance to the large-scale production of hydrogen from water electrolysis. Herein, it is reported that novel $FeNi_3/NiFeO_x$ nanohybrids display high electrocatalytic activities in both hydrogen evolution reaction (HER) and oxygen evolution reaction (OER). These $FeNi_3/NiFeO_x$ nanohybrids are obtained with the unique hydrogenation treatment of $NiFeO_x$ nanosheets. Small onset potentials of ≈20 and 240 mV are obtained for HER and OER, respectively, benefited from the synergistic effect of $FeNi_3$ and $NiFeO_x$. Only a small voltage of 1.55 V is needed to reach a current density of 10 mA cm^{-2} for the overall water splitting in an alkaline electrolyzer when using $FeNi_3/NiFeO_x$ as both cathode and anode catalysts. This is one of the best performance of electrocatalysts for HER and OER, shining the bright future for earth-abundant, low-cost bifunctional electrocatalysts for large-scale production of hydrogen from water electrolysis.

1. Introduction

Hydrogen generation through photocatalytic and electrolytic water splitting has attracted tremendous attention over the past decades,[1–4] as hydrogen is a highly desirable energy carrier for future clean and renewable energy supply. Since the discovery of black titanium dioxide nanomaterials,[1] water splitting over photocatalysis has witnessed great progress with various black titanium dioxide nanomaterials being reported to be highly active toward photocatalytic water splitting.[5,6] However, hydrogen production through photocatalytic water splitting is still far from practical applications due to its low efficiency. Alternatively, sustainable hydrogen production on a large scale can be achieved by electrolytic water splitting using electricity from solar and wind energy.[7] The challenging issue for electrolytic water splitting is the electrode materials. So far, the state-of-the-art electrocatalysts for hydrogen evolution reaction (HER) and oxygen evolution reaction (OER) are platinum and noble metal oxides (e.g., IrO_2 and RuO_2), respectively. However, their scarcity and high cost largely restrict their widespread applications.[8–10] Therefore, developing earth-abundant, low-cost, yet high-activity electrocatalysts is of high interest and significant importance.

The breakthrough in the photocatalytic water splitting was mainly attributed to the structural modification through the introduction of surface disorder and/or surface defect, usually along with the preferably tuned electronic structure.[1,5,6,11] Recently, surface-defective metal oxide synthesized through hydrogenation found potential application in HER, that is, $WO_{2.9}$ derived from WO_3 through hydrogenation achieved a benchmark current density of 10 mA cm^{-2} at a small overpotential of 70 mV in 0.5 M H_2SO_4.[12] Our previous studies found that Co/Co_3O_4 and Ni/NiO core/shell nanohybrids synthesized though hydrogenation of the corresponding metal oxides achieved a benchmark current density of 10 mA cm^{-2} at a small overpotential of 90 and 145 mV, respectively, in 1.0 M KOH.[3,13] On the other hand, a series of electrochemically tuned materials exhibited remarkably enhanced catalytic activities toward electrolytic water splitting.[9,14,15] Especially, electrochemically tuned $NiFeO_x$ exhibited high activity toward both HER and OER.[14] Therefore, structural modification and structural reconstruction open new ways in tuning the HER–OER activity of the existing materials.

Herein, we report on novel 3D $FeNi_3/NiFeO_x$ nanohybrids as bifunctional catalysts for efficient overall water electrolysis. These nanohybrids are derived from single-phase $NiFeO_x$ through hydrogenation. Their catalytic activities can be finely tuned through the hydrogenation conditions. The $FeNi_3/NiFeO_x$ nanohybrids obtained at 250 °C in hydrogen display superior HER and OER activities. They have a small onset potential

X. Yan, Prof. L. Tian, S. Atkins, Prof. X. Chen
Department of Chemistry
University of Missouri – Kansas City
Kansas City, MO 64110, USA
E-mail: chenxiaobo@umkc.edu
Prof. L. Tian
Hubei Collaborative Innovation Center for
Advanced Organochemical Materials
Ministry-of-Education Key Laboratory for
the Synthesis and Applications of Organic Functional Molecules
Hubei University
Wuhan, Hubei 430062, China
K. Li, H. Zhao, Prof. L. Liu
State Key Laboratory of Luminescence and Applications
Changchun Institute of Optics
Fine Mechanics and Physics
Chinese Academy of Sciences
Changchun, Jilin 130033, China
E-mail: liulei@ciomp.ac.cn
Prof. J. Murowchick
Department of Geosciences
University of Missouri – Kansas City
Kansas City, MO 64110, USA

DOI: 10.1002/admi.201600368

(≈20 mV) and a small overpotential (99 mV) at a current density of ≈10 mA cm^{-2} for HER, along with a small overpotential (≈240 mV) at a current density of 10 mA cm^{-2} for OER. With $FeNi_3/NiFeO_x$ as both cathode and anode electrodes, an overall-water-splitting current density of 10 mA cm^{-2} is achieved at a voltage of 1.55 V in an alkaline electrolyzer. This is among the best performance of the electrocatalysts for HER and OER, showing a promising future of earth-abundant, low-cost bifunctional catalysts for practical industrial application. Meanwhile, this study demonstrates hydrogenation treatment as a new approach in developing novel, effective, and bifunctional catalysts for electrocatalytic water splitting.

2. Results and Discussion

2.1. Synthesis and Characterization of $FeNi_3/NiFeO_x$ Hybrid Catalysts

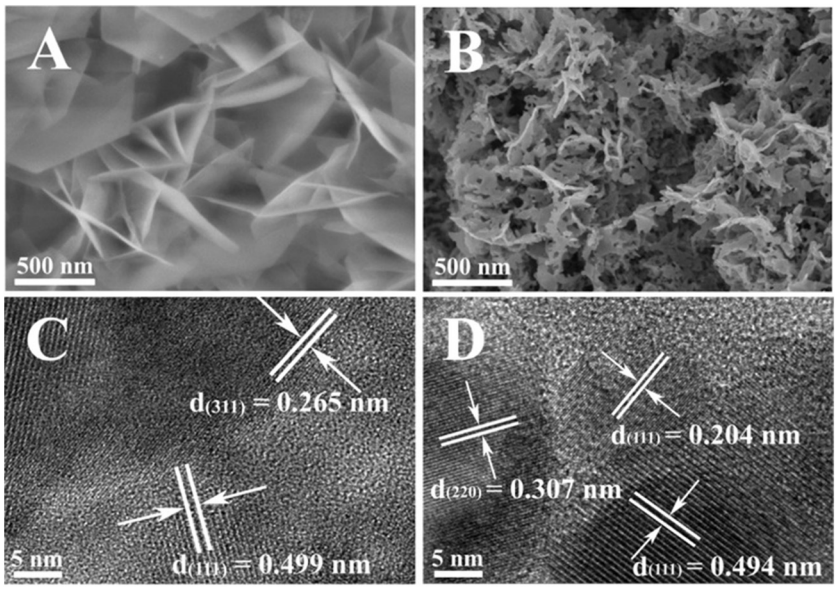

Figure 1. SEM images of A) $NiFeO_x$ and B) $FeNi_3/NiFeO_x$-250, and TEM images of C) $NiFeO_x$ and D) $FeNi_3/NiFeO_x$-250.

A series of $FeNi_3/NiFeO_x$ hybrid catalysts were synthesized from $NiFeO_x$ by hydrogenation at different temperatures in a high-pressure hydrogen atmosphere, and $NiFeO_x$ was synthesized by hydrothermal reaction of iron nitrate, nickel foam, and urea, followed by thermal treatment in air. The nickel foam not only acted as a substrate, but also acted as a Ni source in the reaction due to its oxidation by Fe^{3+} ions in the solution. The urea was decomposed into ammonia during the hydrothermal reaction, which created an alkaline environment, and carbonate, which served as the intercalated anion.[10a] $FeNi_3/NiFeO_x$-250 was selected as the representative hybrid catalyst to investigate the morphology, structure, and composition. For comparison, $NiFeO_x$ was also characterized. X-ray photoelectron spectroscopy (XPS) analyses showed that $NiFeO_x$ and $FeNi_3/NiFeO_x$-250 had an elemental composition of Ni:Fe close to 1:1 (Table S1, Supporting Information). Scanning electron microscope (SEM) image (**Figure 1**A) showed that $NiFeO_x$ existed in the form of nanosheets. The nanosheet morphology was still recognized for $FeNi_3/NiFeO_x$-250 (Figure 1B), but each nanosheet became apparently fractionated due to the hydrogenation reaction. X-ray diffraction (XRD) pattern (Figure S1, Supporting Information) of $NiFeO_x$ matched well with a cubic Fe_2O_3 standard pattern (JCPDS no. 39-1346). This suggested that Ni ions replaced partial ions in the lattice of Fe_2O_3 (Ni-doped Fe_2O_3) and formed $NiFeO_x$ (here $NiFeO_x$ is used to generally reflect the chemical composition of the Ni-doped Fe_2O_3). This was further confirmed by the high resolution transmission electron microscope (HRTEM) observation. In Figure 1C, the *d*-spacing values of 0.265 and 0.499 nm corresponded to the typical (310) and (111) planes of Fe_2O_3, respectively. After hydrogenation, the main phase of $NiFeO_x$ was retained in $FeNi_3/NiFeO_x$-250 as depicted by the XRD pattern (Figure S1, Supporting Information). Newly appeared diffraction peaks at 44.2°, 51.4°, and 75.7° indicated the formation of $FeNi_3$ (JCPDS no. 38-0419). Figure 1D showed the HRTEM image of $FeNi_3/NiFeO_x$-250. The two planes with *d*-spacing of 0.307 and 0.494 nm matched well with the (220) and (111) planes of Fe_2O_3, respectively. The crystalline lattice with a *d*-spacing of 0.204 nm was close to the (111) plane of $FeNi_3$, and the $FeNi_3$ nanocrystal was on the surface of $NiFeO_x$, exposing some $FeNi_3/NiFeO_x$ nanointerfaces.

XPS analyses were performed to estimate the chemical valence of the surface elements. **Figure 2** showed the detailed XPS spectra of $NiFeO_x$ and $FeNi_3/NiFeO_x$-250. The XPS survey spectra of $NiFeO_x$ and $FeNi_3/NiFeO_x$-250 were similar (Figure 2A): signals from Ni, Fe, and O elements were observed. Two core-level signals of Ni in $NiFeO_x$ centered at 855.4 and 873.0 eV (Figure 2B) were ascribed to Ni^{2+} $2p_{3/2}$ and Ni^{2+} $2p_{1/2}$, respectively.[16,17] Signals located at ≈861 and ≈879 eV were the satellite peaks corresponding to Ni^{2+} $2p_{3/2}$ and Ni^{2+} $2p_{1/2}$, respectively.[17] In the Fe 2p spectrum of $NiFeO_x$, the typical core-level signals located at 711.3 and 724.6 eV were derived from the Fe^{3+} $2p_{3/2}$ and Fe^{3+} $2p_{1/2}$, respectively.[18] After hydrogen reduction, the two core-level signals shifted to lower binding energies, namely, 710.3 and 723.8 eV. These signal positions are typical for Fe_3O_4,[19a] indicating the partial reduction of the surface Fe^{3+} ions. Similar O 1s spectra were observed for $NiFeO_x$ and $FeNi_3/NiFeO_x$-250, and they could be deconvoluted into three peaks (Figure 2D). The fitted peaks of $NiFeO_x$ located at 529.3, 530.7, and 532 eV, which were assigned to the lattice O^{2-}, hydroxyl groups and/or oxygen vacancies, and adsorbed water, respectively.[19b–d] These peaks shifted to higher binding energy in $FeNi_3/NiFeO_x$-250, corresponding to 529.6, 530.9, and 532.5 eV. This suggested the environmental change of the oxygen in $FeNi_3/NiFeO_x$-250 owing to the surface structural change after hydrogenation treatment.

2.2. Hydrogen Evolution Reaction of $FeNi_3/NiFeO_x$ Hybrid Catalysts

The HER activities of the $FeNi_3/NiFeO_x$ series were evaluated in 1.0 M KOH by linear sweep voltammetry in a standard

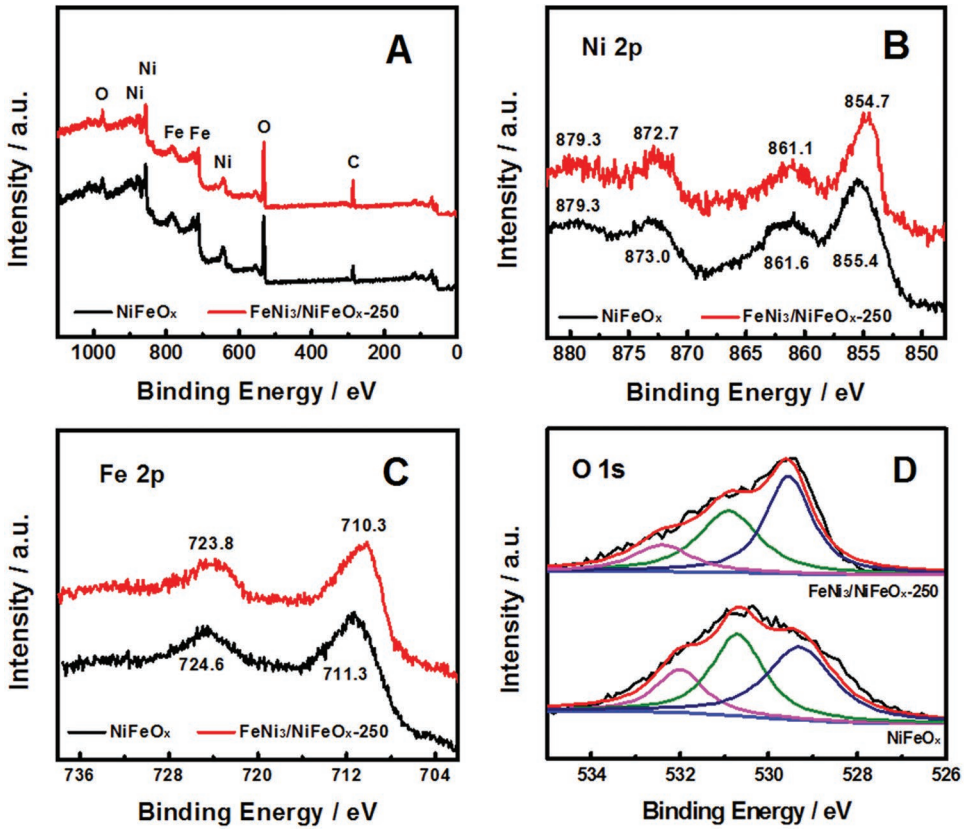

Figure 2. A) XPS survey, and XPS spectra of the B) Ni 2p, C) Fe 2p, and D) O 1s peaks of $NiFeO_x$ (black curves) and $FeNi_3/NiFeO_x$-250 (red curves).

three-electrode system. For comparison, the commercial Pt/C as a benchmark catalyst was electrochemically evaluated under the same condition. The HER activity of the $FeNi_3/NiFeO_x$-250 catalyst was much higher than the bare nickel foam and the pristine $NiFeO_x$ (**Figure 3**A). The $FeNi_3/NiFeO_x$-250 catalyst required a very small overpotential of 99 mV to reach a benchmark current density of 10 mA cm^{-2}. In sharp contrast, a large overpotential (262 mV) was needed for the $NiFeO_x$ catalyst. Meanwhile, the $FeNi_3/NiFeO_x$-250 catalyst showed a very small onset potential (≈20 mV), which was comparable to the state-of-the-art catalyst Pt/C. Therefore, $FeNi_3/NiFeO_x$-250 was among the best first-row transition metal oxide based catalysts in alkaline electrolytes. For example, the HER activity of $FeNi_3/NiFeO_x$-250 was significantly higher than that of cobalt–cobalt oxide/N-doped carbon hybrids (10 mA cm^{-2} at 260 mV overpotential in 1 M KOH),[20a] and was comparable to nickel oxide/nickel–carbon nanotube composites (10 mA cm^{-2} at ≈85 mV overpotential in 1 M KOH).[21] Catalyst stability was investigated by chronoamperometry. Current–time characteristic curve of the $FeNi_3/NiFeO_x$-250 catalyst at an overpotential of 170 mV showed negligible current degradation (Figure 3B), indicative of a robust durability. The remarkably enhanced HER performance confirmed the efficacy of high-pressure hydrogen reduction on Ni–Fe oxide, and was in accord with the discoveries that metal–metal oxide heterostructures are highly active toward HER.[3,13,20,21]

For $FeNi_3/NiFeO_x$-250 and $FeNi_3/NiFeO_x$-300, a reduction peak was observed prior to hydrogen evolution (Figure 3A,C). Similar reduction peak was commonly observed in amorphous or defect-rich materials.[3,22a,b] This reduction peak may be originated from the reduction of some unstable species on the surface, such as amorphous phase. It is more likely derived from the defects. To have more insightful information, much more work needs to be done in the future.

In order to understand how the structure change is correlated with the HER activity, the structural evolution with reaction temperature was directly investigated by XRD. XRD patterns (Figure S2, Supporting Information) suggested that the content of $FeNi_3$ alloy increased with increasing the hydrogenation temperature, along with the depletion of $NiFeO_x$ as evidenced by the continuously weakened diffraction peaks. The HER activities of the $FeNi_3/NiFeO_x$ series were highly dependent on their structural change during the hydrogenation process. The overpotential required to reach a current density of 10 mA cm^{-2} increased in the sequence of $FeNi_3/NiFeO_x$-250 (99 mV) < $FeNi_3/NiFeO_x$-300 (174 mV) < $FeNi_3/NiFeO_x$-200 (187 mV) < $NiFeO_x$ (262 mV) (Figure 3C). The excellent HER activity of $FeNi_3/NiFeO_x$-250 was attributed to the newly generated $FeNi_3/NiFeO_x$ interface.[3,13,20,21] Given that $FeNi_3/NiFeO_x$-200 was absent of Ni–Fe alloy, it was suggested that the hydrogenated $NiFeO_x$ intrinsically had higher HER activity than pristine $NiFeO_x$ due to the generation of surface defects from hydrogenation. Previous researches have showed that hydrogenated metal oxides had a defect-rich surface.[3,13,23] Our XPS investigation also revealed that $FeNi_3/NiFeO_x$-250 had a more complicated surface environment than pristine $NiFeO_x$. A defect-rich surface was believed to expose more active sites

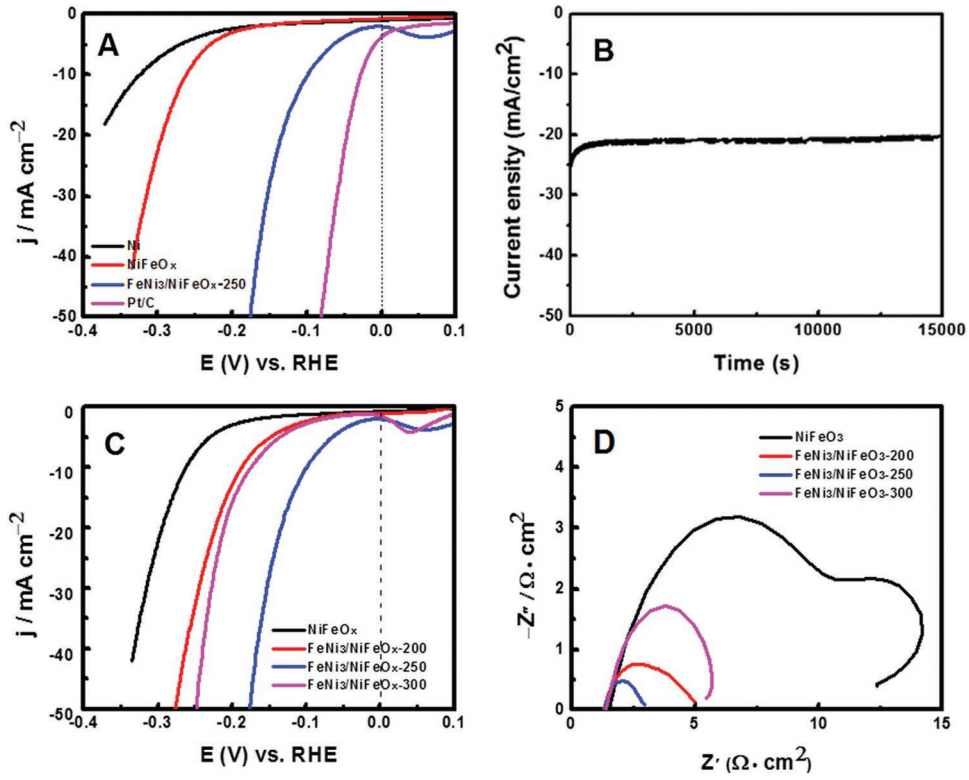

Figure 3. Electrochemical characterization of hydrogen evolution reaction. A) Polarization curves of $NiFeO_x$ and $FeNi_3/NiFeO_x$-250 in 1 M KOH at a scan rate of 5 mV s^{-1}. B) Current–time characteristics of $FeNi_3/NiFeO_x$-250 at an overpotential of 170 mV without *iR*-compensation. C) Comparative studies of pristine $NiFeO_x$ and $FeNi_3/NiFeO_x$ series in 1 M KOH at a scan rate of 5 mV s^{-1}. D) Nyquist plots of pristine $NiFeO_x$ and $FeNi_3/NiFeO_x$ series at −0.2 V versus RHE.

for HER.[3,4a,12,13,22] For example, sulfur or oxygen vacancies can greatly enhance the HER activity of MoS_2 or WO_3.[4a,12] On the other hand, Ni–Fe alloy itself has a low HER activity.[24] Therefore, the superior HER activity of $FeNi_3/NiFeO_x$-250 was likely derived from the synergistic effect of the surface-defective $NiFeO_x$ and $FeNi_3$ alloy. Compared with $FeNi_3/NiFeO_x$-250, $FeNi_3/NiFeO_x$-300 had a much worse HER activity. This was likely caused by the overhydrogenation, which led to the sharp decrease of $NiFeO_x$ (Figure S2, Supporting Information) and thus markedly diminished metal/metal oxide interface (this was verified by the sharp decrease of its electrochemical surface area (ECSA) discussed below). Therefore, a well-balanced combination of metal and surface-defective metal oxide that brought about the maximized metal/metal oxide interfaces was likely critical to the optimum HER activity.

To reveal the influence of surface area, the relative ECSA of the catalysts was estimated to fully understand structure–activity relationship. Solving for the exact surface area is difficult due to the unknown capacitive behavior of the electrodes. Instead, the ECSA values of the catalysts were estimated from the double layer capacitance (C_{dl}), as C_{dl} is linearly proportional to effective active surface area.[13,25] The linear slope of the capacitive current against scan rate was used to represent the ECSA. As shown in Figure S3A (Supporting Information), the ECSA increased in the sequence of $FeNi_3/NiFeO_x$-300 < $FeNi_3/NiFeO_x$-200 < $NiFeO_x$ < $FeNi_3/NiFeO_x$-250. The nonmonotonous variation of ESCA over hydrogenation temperature was probably related to the metal/metal oxide interface. $FeNi_3/NiFeO_x$-250 had the largest metal/metal oxide interface, while $FeNi_3/NiFeO_x$-200 had no metal/metal oxide interface. The very small ECSA of $FeNi_3/NiFeO_x$-300 was owed to the rapidly diminished metal/metal oxide interface owing to the overhydrogenation. Current density at overpotential of 150 mV was plotted against ESCA ($2C_{dl}$) (Figure S3B, Supporting Information) to obtain more insightful information. There was no straightforward correlation between HER activity and ECSA. The ECSA of $NiFeO_x$ was more than two times that of $FeNi_3/NiFeO_x$-200, but the latter exhibited a much higher HER activity. This again suggested that the defect-rich surface intrinsically had a high HER activity. $FeNi_3/NiFeO_x$-300 exhibited a slightly smaller ECSA than $FeNi_3/NiFeO_x$-200, but displayed a slightly higher HER activity. This indicated the importance of the $FeNi_3$ alloy. Hence, these results were explained with the exposed metal/metal oxide interface, along with numerous defects on the surface of metal oxide, in enhancing the HER activity. This is consistent with previous observations.[4a,12,20a,b,21] For example, oxygen or sulfur vacancies have been shown to greatly enhance the HER activity of WO_3 by hydrogenation[12] and in MoS_2,[4a] and the synergistic effect of metal/metal oxide interfaces have been demonstrated with improved HER activities.[20a,b,21]

To reveal the HER kinetics on the surface of the catalysts, electrochemical impedance spectroscopy (EIS) analyses were performed at −0.2 V versus reversible hydrogen electrode (RHE).

According to the Nyquist plots (Figure 3D), $NiFeO_x$ presented a different hydrogen evolution mechanism from the $FeNi_3$/$NiFeO_x$ series. Two semicircles in the Nyquist plot of $NiFeO_x$ indicated a two-time-constant behavior. One semicircle suggested a one-time-constant behavior for the $FeNi_3/NiFeO_x$ series. This was further confirmed by the Bode plots (Figure S4, Supporting Information). High-frequency semicircle is associated with the charge transfer resistance (R_{ct}) or the electrocatalytic kinetics.[20a,22c] $NiFeO_x$ had the largest R_{ct} (8.8 Ω), followed by $FeNi_3/NiFeO_x$-300 (4.4 Ω), $FeNi_3/NiFeO_x$-200 (3.9 Ω), and $FeNi_3$/$NiFeO_x$-250 (2.0 Ω). The largely reduced R_{ct} for the $FeNi_3/NiFeO_x$ series indicated a much faster reaction rate. This was in agreement with the catalytic activities of the as-prepared materials.

In alkaline media, two mechanisms were developed to explain the HER pathway: Volmer–Heyrovesky (1) or Volmer–Tafel (2) processes[20a,21,26]

$$\begin{aligned} &H_2O + e^- \rightarrow H_{ad} + OH^- \text{ (Volmer)} \\ &H_2O + H_{ad} + e^- \rightarrow H_2 + OH^- \text{ (Heyrovesky)} \end{aligned} \quad (1)$$

$$\begin{aligned} &H_2O + e^- \rightarrow H_{ad} + OH^- \text{ (Volmer)} \\ &H_{ad} + H_{ad} \rightarrow H_2 \text{ (Tafel)} \end{aligned} \quad (2)$$

Tafel slope of 120, 40, or 30 mV dec^{-1} was expected if the Volmer, Heyrovsky, or Tafel step is the rate-determining step, respectively.[26] Tafel plot (Figure S5, Supporting Information) showed that the HER mechanism for $FeNi_3/NiFeO_x$-250 followed the Volmer–Heyrovesky pathway. Both Volmer and Heyrovesky processes involved the adsorption of H_2O onto the surface of the catalyst, subsequent electrochemical reduction of the absorbed H_2O to form adsorbed H atom and OH^- group, desorption of OH^- to refresh the surface, and formation of H_2 from absorbed H atom. Therefore, the formation and desorption of OH^- in both Volmer and Heyrovesky processes likely determine the overall water splitting rate. It was reported that the surface defects of metal oxides were favorable for the dissociative adsorption of water molecules.[12,27] Therefore, surface-defective $NiFeO_x$ could facilitate both Volmer and Heyrovesky processes. This explains the improved catalytic activity of $FeNi_3/NiFeO_x$-200. The introduction of $FeNi_3$ could further facilitate the electrochemical reduction of the absorbed H_2O, as Ni was calculated to have suitable H binding energy close to Pt[21] and metal/metal oxide interface was believed to lower the energy barrier of water dissociation.[20b] Therefore, the Volmer process was further enhanced by the $FeNi_3$ alloy, thus leading to the much higher catalytic activity of $FeNi_3/NiFeO_x$-250 versus $FeNi_3/NiFeO_x$-200. In a word, the OH^- generated by H_2O splitting might preferentially attach to a surface-defective $NiFeO_x$ site near the $FeNi_3/NiFeO_x$ interface due to the strong electrostatic affinity to the positively charged metal ions and more unfilled d orbitals in metal ions,[20a,21] while a nearby $FeNi_3$ site would facilitate H adsorption and electron transfer, imparting synergistic HER activity to $FeNi_3/NiFeO_x$.

2.3. Oxygen Evolution Reaction of $FeNi_3/NiFeO_x$ Hybrid Catalysts

The OER activities of the $FeNi_3/NiFeO_x$ hybrid catalysts were also investigated in 1 M KOH electrolyte using linear sweep voltammetry. As a blank control, bare nickel foam had a very low OER activity (**Figure 4**A). For comparison, the polarization curves of $NiFeO_x$ and IrO_2 were provided in Figure 4A. $NiFeO_x$ nanosheets demonstrated a high OER activity similar to the standard catalyst IrO_2. In detail, $NiFeO_x$ nanosheets had a small onset potential of ≈1.49 V versus RHE and a small overpotential (285 mV) to reach a critical current density of ≈10 mA cm^{-2}. This also confirmed the existence of $NiFeO_x$ as neither NiO[7b,28b] nor Fe_2O_3[29a] was very active toward OER. The OER performance of $NiFeO_x$ nanosheets was better than the reported $NiFeO_x$ (10 mA cm^{-2} at 350 mV overpotential[28]). This can be attributed to (I) the 3D nature of our electrode and open space between nanosheets which can facilitate the diffusion of electrolyte and hydrogen bubbles; (II) the large surface area associated with the nanostructured nanosheets along with the absence of binder, accelerating the surface reaction; and (III) the direct contact of the nanosheets to the underneath conductive substrate which ensured each nanosheet to participate in the reaction. Excitingly, the $FeNi_3/NiFeO_x$ hybrid catalysts showed even more superior catalytic activities. They presented a similar onset potential of ≈1.47 V versus RHE at which an absolute OER current of ≈0.5 mA cm^{-2} was achieved (Figure S6,

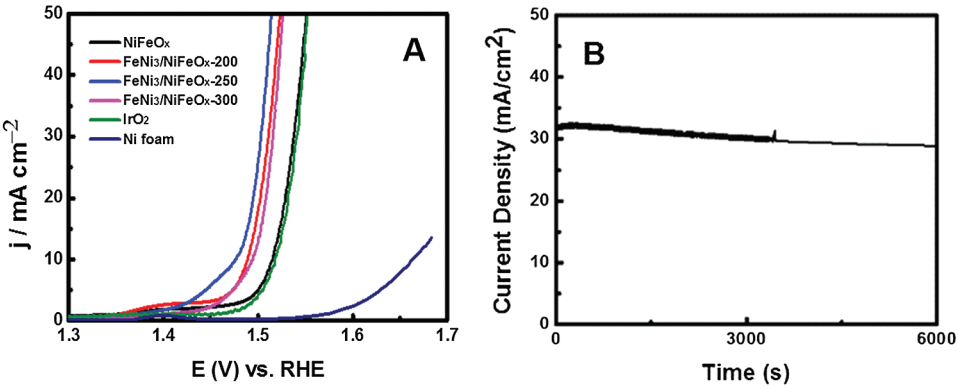

Figure 4. Electrochemical characterization of oxygen evolution reaction. A) Polarization curves of IrO_2, $NiFeO_x$, and the $FeNi_3/NiFeO_x$ series in 1 M KOH at a scan rate of 5 mV s^{-1}. B) Current–time characteristics of $FeNi_3/NiFeO_x$-250 at an overpotential of 330 mV without *iR*-correction.

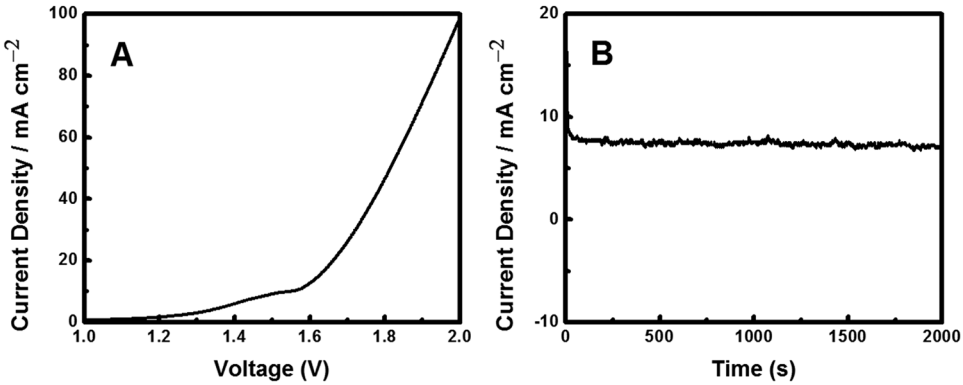

Figure 5. Overall water-splitting characteristics of two different $FeNi_3/NiFeO_x$-250 catalyst electrodes in a two-electrode configuration in 1 M KOH. All the data are without *iR*-correction. A) Polarization curve at a scan rate of 5 mV s^{-1}. B) Current–time characteristics at a voltage of 1.60 V.

Supporting Information). A much smaller overpotential was needed to approach ≈10 mA cm^{-2}: 258 mV for $FeNi_3/NiFeO_x$-200, 246 mV for $FeNi_3/NiFeO_x$-250, and 263 mV for $FeNi_3/NiFeO_x$-300. The higher OER activities of the $FeNi_3/NiFeO_x$ series were proposed due to the surface defects, which was consistent with previous reports that amorphous or defective Ni–Fe oxides had higher OER activities.[29] The superior OER activity of $FeNi_3/NiFeO_x$-250 was further ascribed to its larger ECSA or more exposed surface defects. In alkaline electrolytes, oxidation of four OH^- groups were transformed into H_2O and O_2 by losing a total of four electrons[30]

$$4OH^- \leftrightarrow 2H_2O + O_2 + 4e^- \quad (3)$$

This process involved the adsorption of OH^- group and a four-electron oxidation process. Appropriate interaction between catalyst surface and oxygen,[30,31] and good electrical conductivity[32] were two important parameters for an excellent OER catalyst. As discussed above, the defect-rich surface favored the formation and desorption of OH^- and as well displayed a very small R_{ct}, thus synergistically resulting in a high catalytic activity toward OER. Recent studies also proved that vacancies could highly enhance the water oxidation process.[33] The OER durability of $FeNi_3/NiFeO_x$-250 was evaluated using chronoamperometry without *iR*-compensation. As shown in Figure 4B, the current density showed a negligible degradation during a long period of 6000 s. This suggested that $FeNi_3/NiFeO_x$-250 had an excellent durability toward OER.

2.4. Overall Water Splitting of $FeNi_3/NiFeO_x$ Hybrid Catalysts

An electrolyzer was assembled to estimate the actual catalytic activity of $FeNi_3/NiFeO_x$-250 toward overall water splitting in 1 M KOH. A current density of 10 mA cm^{-2} was achieved at a voltage of 1.55 V (**Figure 5**A). The electrolyzer reached ≈100 mA cm^{-2} at 2.0 V. This again confirmed the superior activity of $FeNi_3/NiFeO_x$-250 toward HER and OER. The durability of the electrolyzer, which is of great importance for the practical applications, was carried out at 1.6 V in 1 M KOH at room temperature. Negligible degradation was observed in current density (Figure 5B). Thus, the excellent performance made $FeNi_3/NiFeO_x$-250 an attractive earth-abundant bifunctional electrocatalyst for water splitting.

3. Conclusion

In summary, we report a 3D $FeNi_3/NiFeO_x$ nanohybrids as highly active bifunctional electrocatalyst for overall water splitting in alkaline electrolyte. Their properties can be finely tuned with hydrogenation to obtain high HER and OER activities. A small onset potential of ≈20 and 240 mV is obtained for HER and OER, respectively. The high activity can be attributed to the synergistic effect of the $FeNi_3$ alloy and surface-defective $NiFeO_x$. An overall-water-splitting current density of 10 mA cm^{-2} is achieved at a voltage of 1.55 V with $FeNi_3/NiFeO_x$ as both cathode and anode catalysts. The current reaches ≈100 mA cm^{-2} at 2.0 V, displaying a promising future for practical industrial hydrogen production. This finding may open a new door to the design and fabrication of earth-abundant, low-cost bifunctional metal oxide electrocatalysts for water splitting.

4. Experimental Section

Synthesis: In a typical synthesis, a piece of nickel foam (1 cm × 3 cm) was sonicated in a 3 M HCl solution for 10 min to remove the possible surface oxide layer. After rinsed with deionized water, the nickel foam was transferred into a solution with 0.5 mmol of iron(III) nitrate nonahydrate ($Fe(NO_3)_3{\cdot}9H_2O$) and 2.5 mmol urea in 16 mL water, and followed by a hydrothermal treatment at 120 °C for 12 h. A small amount of metal Ni on the surface of the Ni substrate was oxidized by Fe^{3+} ions in the solution to generate Ni^{2+} ions as the nickel source for the product. After cooled down to room temperature, the nickel foam was washed with deionized water, dried in air, and annealed at 300 °C for 2 h in air to obtain $NiFeO_x$. Finally, $FeNi_3/NiFeO_x$ nanohybrids were obtained by heating at 200, 250, and 300 °C for 3 h in a high-pressure hydrogen atmosphere (hydrogenation), labeled as $FeNi_3/NiFeO_x$-200, $FeNi_3/NiFeO_x$-250, and $FeNi_3/NiFeO_x$-300, respectively. In order to facilitate the investigation of the structural evolution of the $NiFeO_x$ with the increase of the hydrogenation temperature, similar processes were also applied to the powders collected from the reaction solution.

Characterization: Morphological structures of the samples were examined using EM and TEM. The SEM images were taken on a Hitachi 4800 field emission SEM. The foams were directly mounted on the sample stage for analysis. The TEM study was performed on a FEI

Tecnai F20 STEM. The electron accelerating voltage was 200 kV. A small amount of powder sample dispersed in water was dropped onto a thin holey carbon film, and dried overnight before TEM measurement. Lattice structural and chemical properties were investigated using XRD and XPS. The XRD was performed on a Rigaku Miniflex X-ray diffractometer using Cu Kα radiation (wavelength = 1.5418 Å). XPS data were collected using a Kratos Axis 165 X-ray photoelectron spectrometer. Spectra were acquired using a photon beam of 1486.6 eV, selected from an Al/Mg dual-anode X-ray source.

Electrochemical Measurement: Electrochemical measurements were carried out in a three-electrode system at room temperature. The nickel foams covered with samples were directly used as the working electrodes. A Pt wire and an Ag/AgCl electrode were used as the counter and reference electrodes, respectively. A 1.0 M KOH solution was used as the electrolyte. Cyclic voltammetry measurement was performed five cycles in the voltage range of 0.0–0.5 V versus Ag/AgCl at a scan rate of 5 mV s^{-1} to activate the working electrodes. Linear sweep voltammetry was performed at a scan rate of 5 mV s^{-1} to evaluate the HER performance of the catalysts. EIS analysis was carried out using a 10 mV amplitude AC signal over a frequency range from 100 kHz to 10 mHz on a Biologic potentiostat/EIS electrochemical workstation. The polarization curves were *iR*-corrected for an ohmic drop according to the EIS Nyquist plots. The reference electrode was calibrated against and concerted to reversible hydrogen electrode. The calibration was performed in the high purity hydrogen saturated 1 M KOH electrolyte with a Pt wire as the working electrode. In order to estimate the relative electrochemical surface area of the catalysts, C_{dl} of each catalyst was measured using a simple cyclic voltammetry method. The voltage window of cyclic voltammograms was 0.1–0.2 V versus RHE. The scan rates were 20, 40, 60, 80, and 100 mV s^{-1}. C_{dl} was estimated by plotting the Δj ($j_a - j_c$) at 0.15 V versus RHE against the scan rate, where the slope was twice the C_{dl}.[13,25]

Supporting Information

Supporting Information is available from the Wiley Online Library or from the author.

Acknowledgements

X.C. acknowledges the support from the College of Arts and Sciences, University of Missouri – Kansas City, the University of Missouri Research Board (UMRB), and the University of Missouri Interdisciplinary Intercampus (IDIC) Programs. X.Y. thanks the funds provided by the University of Missouri – Kansas City, School of Graduate Studies. L.T. thanks the National Natural Science Foundation of China (No. 51302072) and the China Scholarship Council for their financial supports. L.L. acknowledges the support of the National Natural Science Foundation of China (No. 11174273).

Received: May 2, 2016
Revised: July 20, 2016
Published online: September 7, 2016

[1] X. Chen, L. Liu, P. Y. Yu, S. S. Mao, *Science* **2011**, *331*, 746.
[2] X. Chen, S. Shen, L. Guo, S. S. Mao, *Chem. Rev.* **2010**, *110*, 6503.
[3] X. Yan, L. Tian, M. He, X. Chen, *Nano Lett.* **2015**, *15*, 6015.
[4] a) D. Kong, H. Wang, Z. Lu, Y. Cui, *J. Am. Chem. Soc.* **2014**, *136*, 4897; b) H. Li, C. Tsai, A. L. Koh, L. Cai, A. W. Contryman, A. H. Fragapane, J. Zhao, H. S. Han, H. C. Manoharan, F. Abild-Pedersen, J. K. Nørskov, X. Zheng, *Nat. Mater.* **2016**, *15*, 48.
[5] N. Liu, C. Schneider, D. Freitag, M. Hartmann, U. Venkatesan, J. Müller, E. Spiecker, P. Schmuki, *Nano Lett.* **2014**, *14*, 3309.
[6] a) G. Wang, H. Wang, Y. Ling, Y. Tang, X. Yang, R. C. Fitzmorris, C. Wang, J. Z. Zhang, Y. Li, *Nano Lett.* **2011**, *11*, 3026; b) W. Zhou, W. Li, J.-Q. Wang, Y. Qu, Y. Yang, Y. Xie, K. Zhang, L. Wang, H. Fu, D. Zhao, *J. Am. Chem. Soc.* **2014**, *136*, 9280; c) Z. Wang, C. Yang, T. Lin, H. Yin, P. Chen, D. Wan, F. Xu, F. Huang, J. Lin, X. Xie, M. Jiang, *Adv. Funct. Mater.* **2013**, *23*, 5444; d) H. Cui, W. Zhao, C. Yang, H. Yin, T. Lin, Y. Shan, Y. Xie, H. Gu, F. Huang, *J. Mater. Chem. A* **2014**, *2*, 8612; e) Z. Wang, C. Yang, T. Lin, H. Yin, P. Chen, D. Wan, F. Xu, F. Huang, J. Lin, X. Xie, M. Jiang, *Energy Environ. Sci.* **2013**, *6*, 3007.
[7] a) J. Luo, J.-H. In, M. T. Mayer, M. Schreier, M. K. Nazeeruddin, N.-G. Park, S. D. Tilley, J. F. Fan, M. Grätzel, *Science* **2014**, *345*, 1593; b) L.-A. Stern, X. Hu, *Faraday Discuss.* **2014**, *176*, 363.
[8] a) J. Tian, Q. Liu, Y. Liang, Z. Xing, A. M. Asiri, X. Sun, *ACS Appl. Mater. Interfaces* **2014**, *6*, 20579; b) D. Kong, J. J. Cha, H. Wang, H. R. Lee, Y. Cui, *Energy Environ. Sci.* **2013**, *6*, 3553.
[9] Y. Liu, H. Wang, D. Lin, C. Liu, P.-C. Hsu, W. Liu, W. Chen, Y. Cui, *Energy Environ. Sci.* **2015**, *8*, 1719.
[10] a) Z. Lu, W. Xu, W. Zhu, Q. Yang, X. Lei, J. Liu, Y. Li, X. Sun, X. Duan, *Chem. Commun.* **2014**, *50*, 6479; b) L. Qian, Z. Lu, T. Xu, X. Wu, Y. Tian, Y. Li, Z. Huo, X. Sun, X. Duan, *Adv. Energy Mater.* **2015**, *5*, 1500245.
[11] a) L. Liu, P. Y. Yu, X. Chen, S. S. Mao, D. Z. Shen, *Phys. Rev. Lett.* **2012**, *111*, 065505; b) X. Chen, L. Liu, Z. Liu, M. A. Marcus, W.-C. Wang, N. A. Oyler, M. E. Grass, B. Mao, P.-A. Glans, P. Y. Yu, J. Guo, S. S. Mao, *Sci. Rep.* **2013**, *3*, 1510; c) A. Naldoni, M. Allieta, S. Santangelo, M. Marelli, F. Fabbri, S. Cappelli, C. L. Bianchi, R. Psaro, V. D. Santo, *J. Am. Chem. Soc.* **2012**, *134*, 7600.
[12] Y. H. Li, P. F. Liu, L. F. Pan, H. F. Wang, Z. Z. Yang, L. R. Zheng, P. Hu, H. J. Zhao, L. Gu, H. G. Yang, *Nat. Commun.* **2015**, *6*, 8064.
[13] X. Yan, L. Tian, X. Chen, *J. Power Sources* **2015**, *300*, 336.
[14] H. Wang, H.-W. Lee, Y. Deng, Z. Lu, P.-C. Hsu, Y. Liu, D. Lin, Y. Cui, *Nat. Commun.* **2015**, *6*, 7261.
[15] a) H. Wang, Z. Lu, D. Kong, J. Sun, T. M. Hymel, Y. Cui, *ACS Nano* **2014**, *8*, 4940; b) H. Wang, Z. Lu, S. Xu, D. Kong, J. J. Cha, G. Zheng, P.-C. Hsu, K. Yan, D. Bradshaw, F. B. Prinz, Y. Cui, *Proc. Natl. Acad. Sci. USA* **2013**, *110*, 19701; c) Z. Lu, H. Wang, D. Kong, K. Yan, P.-C. Hsu, G. Zheng, H. Yao, Z. Liang, X. Sun, Y. Cui, *Nat. Commun.* **2014**, *5*, 4345.
[16] K. K. Lian, D. W. Kirk, S. J. J. Thorpe, *J. Electrochem. Soc.* **1995**, *142*, 3704.
[17] A. Mansour, *Surf. Sci. Spectra* **1994**, *3*, 231.
[18] a) B. J. Tan, K. J. Klabunde, P. M. A. Sherwood, *Chem. Mater.* **1990**, *2*, 186; b) K. Fominykh, P. Chernev, I. Zaharieva, J. Sicklinger, G. Stefanic, M. Döblinger, A. Müller, A. Pokharel, S. Böcklein, C. Scheu, T. Bein, D. Fattakhova-Rohlfing, *ACS Nano* **2015**, *9*, 5180.
[19] a) B. J. Tan, K. J. Klabunda, P. M. A. Sherwood, *Chem. Mater.* **1990**, *2*, 186; b) W. D. Chemelewski, H.-C. Lee, J.-F. Lin, A. J. Bard, C. B. Mullins, *J. Am. Chem. Soc.* **2014**, *136*, 2843; c) M. Chen, Y. Wu, Y. Han, X. Lin, J. Sun, W. Zhang, R. Cao, *ACS Appl. Mater. Interfaces* **2015**, *7*, 21852.
[20] a) H. Jin, J. Wang, D. Su, Z. Wei, Z. Pang, Y. Wang, *J. Am. Chem. Soc.* **2015**, *137*, 2688; b) Z. Weng, W. Liu, L.-C. Yin, R. Fang, M. Li, E. Altman, Q. Fan, F. Li, H.-M. Cheng, H. Wang, *Nano Lett.* **2015**, *15*, 7704.
[21] M. Gong, W. Zhou, M.-C. Tsai, J. Zhou, M. Guan, M.-C. Lin, B. Zhang, Y. Hu, D.-Y. Wang, J. Yang, S. J. Pennycook, B.-J. Hwang, H. Dai, *Nat. Commun.* **2014**, *5*, 4695.
[22] a) D. Merki, S. Fierro, H. Vrubel, X. Hu, *Chem. Sci.* **2011**, *2*, 1262; b) H. Vrubel, D. Merki, X. Hu, *Energy Environ. Sci.* **2012**, *5*, 6136;

c) J. Xie, H. Zhang, S. Li, R. Wang, X. Sun, M. Zhou, J. Zhou, X. W. Lou, Y. Xie, *Adv. Mater.* **2013**, *25*, 5807.
[23] a) T. Xia, P. Wallenmeyer, A. Anderson, J. Murowchick, L. Liu, X. Chen, *RSC Adv.* **2014**, *4*, 41654; b) T. Zhai, S. Xie, M. Yu, P. Fang, C. Liang, X. Lu, Y. Tong, *Nano Energy* **2014**, *8*, 255; c) T. Xia, W. Zhang, W. Li, N. A. Oyler, G. Liu, X. Chen, *Nano Energy* **2013**, *2*, 826.
[24] I. Arul Raj, K. I. Vasu, *J. Appl. Electrochem.* **1990**, *20*, 32.
[25] a) F. Song, X. Hu, *Nat. Commun.* **2014**, *5*, 4477; b) M. A. Lukowski, A. S. Daniel, F. Meng, A. Forticaux, L. Li, S. Jin, *J. Am. Chem. Soc.* **2013**, *135*, 10274.
[26] M. A. Domínguez-Crespo, A. M. Torres-Huerta, B. Brachetti-Sibaja, A. Flores-Vela, *Int. J. Hydrogen Energy* **2011**, *36*, 135.
[27] a) R. Subbaraman, D. Tripkovic, D. Strmcnik, K. C. Chang, M. Uchimura, A. P. Paulikas, V. Stamenkovic, N. M. Markovic, *Science* **2011**, *334*, 1256; b) Y. F. Xu, M. R. Gao, Y. R. Zheng, J. Jiang, S. H. Yu, *Angew. Chem., Int. Ed.* **2013**, *52*, 8546.
[28] a) M. D. Merrill, R. C. Dougherty, *J. Phys. Chem. C* **2008**, *112*, 3655; b) C. C. L. McCrory, S. Jung, J. C. Peters, T. F. Jaramillo, *J. Am. Chem. Soc.* **2013**, *135*, 16977.
[29] a) R. D. L. Smith, M. S. Prévot, R. D. Fagan, Z. Zhang, P. A. Sedach, M. K. J. Siu, S. Trudel, C. P. Berlinguette, *Science* **2013**, *340*, 60; b) M. W. Louie, A. T. Bell, *J. Am. Chem. Soc.* **2013**, *135*, 12329.
[30] J. Suntivich, K. J. May, H. A. Gasteiger, J. B. Goodenough, Y. Shao-Horn, *Science* **2011**, *334*, 1383.
[31] G. Mattioli, P. Giannozzi, A. A. Bonapasta, L. Guidoni, *J. Am. Chem. Soc.* **2013**, *135*, 15353.
[32] a) Y. Li, P. Hasin, Y. Wu, *Adv. Mater.* **2010**, *22*, 1926; b) Z. Peng, D. Jia, A. M. Al-Enizi, A. A. Elzatahry, G. Zheng, *Adv. Energy Mater.* **2015**, *5*, 1402031.
[33] a) Y. Liu, H. Cheng, M. Lyu, S. Fan, Q. Liu, W. Zhang, Y. Zhi, C. Wang, C. Xiao, S. Wei, B. Ye, Y. Xie, *J. Am. Chem. Soc.* **2014**, *136*, 15670; b) J. Bao, X. Zhang, B. Fan, J. Zhang, M. Zhou, W. Yang, X. Hu, H. Wang, B. Pan, Y. Xie, *Angew. Chem., Int. Ed.* **2015**, *54*, 7399.